JOURNAL OF SPACECRAFT AND ROCKETS
Vol. 33, No. 4, July–August 1996

Numerical Study of Multidirectional-Curvature Waverider with Finlets

Sheam-Chyun Lin* and Ming-Chiou Shen†
National Taiwan Institute of Technology, Taipei 10772, Taiwan, Republic of China

A comprehensive numerical study is performed for the flowfields associated with multidirectional-curvature waveriders with finlets. This hypersonic vehicle, composed of an airframe and reflexed trailing edge, is developed by means of the waverider concept. The airframe and finlets can be constructed simultaneously by making an appropriate selection of a freestream trailing-edge curve. In this study, a three-dimensional grid system generated by elliptic differential equations is developed. Additionally, the Navier–Stokes equations with a flux-difference splitting numerical method are utilized to simulate the flowfields associated with the design and off-design flight conditions. At the design Mach number 4, the inviscid numerical results are compared with analytical estimates; in addition, the viscous effects for aerodynamic performance are evaluated. Also, an investigation is made of the variation in aerodynamic performance caused by altering the flight Mach number from 2 to 6. Moreover, the influence on aerodynamic performance and stability of the addition of finlets is discussed in detail.

Nomenclature

$\bar{C}_f$ = average skin-friction coefficient, D_f/qS_b
C_p = pressure coefficient, $p - p_\infty/q$
D = total drag; coefficient $C_D = D/qS_b$
D_w = wave drag, N
i, j, k = grid indices
L = total lift; coefficient $C_L = L/qS_b$
l = length of right circular cone, m
l_w = length of waverider, m
M = Mach number
m = characteristic of longitudinal curvature
n = characteristic of transverse curvature
p = pressure, Pa
q = dynamic pressure, $\rho_\infty V_\infty^2/2$, Pa
R = distance quantities proposed in Ref. 4
Re = Reynolds number, $\rho_\infty V_\infty l_w/\mu_\infty$
S_b = base area, m^2
S_w = wet area, m^2
X, Y = nondimensional Cartesian coordinate system, $x/l\delta$, $y/l\delta$
α = angle of attack, deg
β = semivertex angle of the unperturbed shock, deg
β^* = side angle, deg
Δz_{sm} = static margin proposed in Ref. 5
δ = semivertex angle of the unperturbed cone, deg
ε = perturbation parameter (extremely small)
η_v = volumetric ratio, $V^{2/3}/S_p$
ρ = density, kg/m^3
ϕ_l = azimuthal angle of shock in base plane, deg

Subscripts

c = compression surface quantities
m = mth term in expansion
n = nth term in expansion
0 = zero-order, unperturbed flow quantities
∞ = freestream condition

Received June 3, 1995; revision received March 5, 1996; accepted for publication March 5, 1996.

*Associate Professor, Department of Mechanical Engineering. Member AIAA.
†Graduate Research Assistant, Department of Mechanical Engineering.

Introduction

DURING the past decade, the role of waveriders applied to practical hypersonic vehicles has received considerable interest.[1] The reason is that when a waverider is flying through a hypersonic flow, an attached oblique shock along the leading edge of this configuration will be generated and form a shock layer enclosing the lower surface of the vehicle. Because the high pressure behind the shock wave under the waverider does not leak around the leading edge to the top surface, its lift and lift-to-drag ratio are considerably higher than those of other traditional flight vehicles. In addition, because all of the constituent parts of a waverider belong to a single flowfield, it is possible to take the design of the aircraft (its wings and even the inlets) into consideration at one time without the disadvantages of the conventional approach, in which each part is devised separately and then assembled by a semiempirical method.

In the development of cone-derived waveriders, Rasmussen[2] developed analytical approximate solutions to flowfields of circular and elliptic cones. Those solutions were derived by combining the hypersonic small-disturbance theory with a perturbation method. In 1988, Lin and Rasmussen[3] expanded the circular-cone solution to include the transverse and longitudinal curvatures by a perturbation technique. They also demonstrated that these types of waverider derived from the perturbed flowfields have the advantage of efficient volumetric packaging and enhanced L/D values. This specific solution makes the application of the waveriders more practical and compatible. However, for waveriders to be incorporated into practical aircraft designs, they must be enhanced with control surfaces of various sorts and propulsion units. In view of these needs, several investigations concerning the attachment of the integrated inlets,[4] finlets,[5] and vertical fins[6] on waveriders have been launched. Also, it has been concluded that the effects of finlets are to shift the center of pressure aft and to improve the static stability.[5]

Numerical studies[7–9] have almost always focused on the elliptic-cone waverider (ECDWR) flowfields.[3] Those results provided a sufficient correlation between experimental and analytical results. However, the shock does not attach closely to the wing tip as predicted by the theoretical derivation. Later, the flowfield simulation associated with nonconical waveriders was performed by He and Rasmussen.[10] Shortly thereafter, numerical simulation for a viscous optimized waverider was achieved.[11] Lin and Shen[12] recently performed a numerical simulation for the waverider with transverse and longitudinal curvatures, at design and off-design Mach numbers. They reported that longitudinal curvature would result in an increased lift-to-drag ratio, thereby implying that the waverider has good flight performance at off-design Mach numbers rather than a dramatic degradation.

Until now, computational fluid dynamics investigations involving the waverider flowfields have mostly focused on the forebody. To our knowledge, the waverider configuration integrated with finlets has not yet been studied. It is of interest to examine how the flowfields are changed by the addition of finlets. In this article, numerical simulation is performed for a multidirectional-curvature waverider with finlets (MDCWRF) to satisfy demands for practical applications and examine the accuracy of HSDT. The MDCWRF configuration is generated by using Lin and Rasmussen's approximate solution[3] and selecting a particular freestream trailing-edge curve. Next, Roe's flux-difference-splitting algorithm,[13] together with both the full Navier–Stokes equations and Euler equations, is utilized to solve the inviscid and viscous flowfields for this shape flying at on-design Mach number 4 and off-design Mach numbers 2–6. In addition, the corresponding aerodynamics of the waverider and the influence of an addition of finlets are discussed in detail. This result should be valuable for practical application of waverider-based vehicles.

Airframe and Finlet Generations

The waverider is composed of three surfaces (Fig. 1). Generating a waverider first requires defining two properties: a generating flowfield and a trailing-edge curve. In this work, an approximate analytical solution[3] for a perturbed cone together with a sixth-order freestream trailing-edge curve is chosen to generate the waverider shape with finlets. In spherical coordinates, the perturbed body with combined transverse and longitudinal curvature, as shown in Fig. 2, is represented by

$$\theta = \delta[1 - \varepsilon(r/l)^m \cos n\phi] \tag{1}$$

The transverse curvature is introduced by $\cos n\phi$ in which n is an integer, and $(r/l)^m$ is a function that produces the longitudinal curvature.[6]

In addition, a sixth-order freestream trailing-edge curve[10] can be expressed as

$$X = R_0 + b_2 Y^2 + b_4 Y^4 + b_6 Y^6 \tag{2}$$

The freestream reflexed trailing edge can be determined by applying the reflexed trailing-edge boundary and setting the two extremes

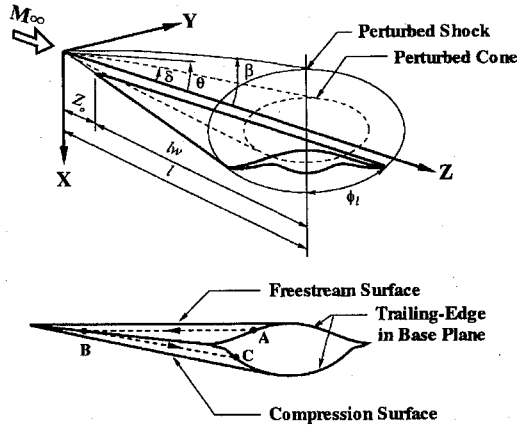

Fig. 1 Construction of configuration and coordinate system.

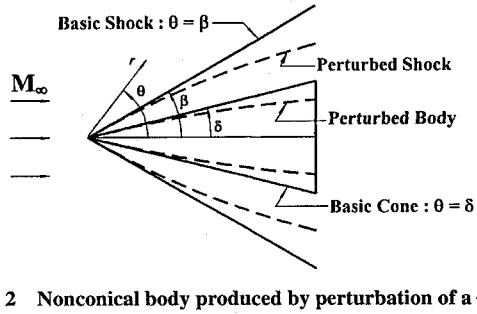

Fig. 2 Nonconical body produced by perturbation of a cone.

Table 1 Design aerodynamic and geometric properties

Flight conditions and shape factors	Design parameters	Aerodynamic properties
$M_\infty = 4.0$	$\delta = 10$	$C_L = 0.6508$
$\alpha = 0$	$\phi_l = 55$	$C_D = 0.0794$
$\beta^* = 0$	$\omega_1 = 0.62$	$\bar{C}_f = 0.0196$
$Re = 3.94 \times 10^6$	$\omega_2 = 0.94$	$(L/D)_{\text{inv}} = 8.198$
Adiabatic wall	$m = 1$	$(L/D)_{\text{vis}} = 6.571$
$S_w = 0.7003$	$n = 2$	$\Delta z_{\text{sm}} = -0.0735$
$S_b = 0.0357$	$\varepsilon = 0.1$	——
$\eta_v = 0.1503$	$R_0 = 0.5X_{\phi_l}$	——

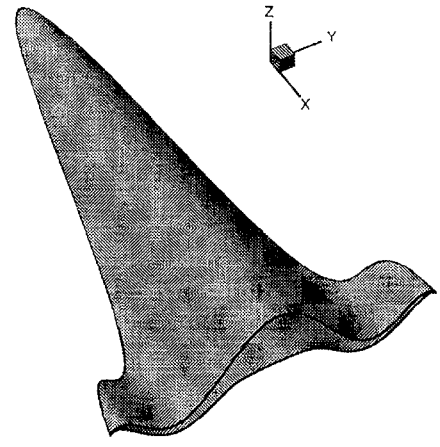

Fig. 3 Mach 4 MDCWRF geometry.

$\omega_1 \equiv Y_1/Y_{\phi_l}$ and $\omega_2 \equiv Y_2/Y_{\phi_l}$ for $X(Y)$ (Ref. 10). Starting with this trailing-edge curve (such as point A in Fig. 1), the corresponding streamlines are traced upstream until they intersect with the bow shock (such as point B in Fig. 1). Thus, the lower surface of a waverider is constructed by tracing the stream surface from the bow shock downstream to the base plane (e.g., point C in Fig. 1).

In addition, by means of the integral momentum equations of inviscid flow, the lift and wave drag forces for the hypersonic vehicle can be expressed in the form[4]

$$L = 4ql^2\delta^2 \int_0^{\phi_l} \int_{\theta_{bc}}^{\beta} \left(\frac{\rho_0}{\rho_\infty} \cos\phi + \varepsilon L^*_{mn} \right) \mathrm{d}\theta_0 \, \mathrm{d}\phi \tag{3}$$

$$D_w = 2ql^2\delta^2 \int_0^{\phi_l} \int_{\theta_{bc}}^{\beta} \left\{ \left[\frac{\rho_0}{\rho_\infty} \left(2 + \ell_v \frac{\beta^2}{\theta_0^2} \right) - \frac{C_{p_0}}{\delta^2} + \varepsilon D^*_{mn} \cos n\phi \right] \theta_0 \right\} \mathrm{d}\theta_0 \, \mathrm{d}\phi \tag{4}$$

As proposed in Ref. 10, an average skin-friction coefficient was selected at an on-design condition to estimate the viscous effect. Also, a wing–body–finlet configuration with a higher lift-to-drag ratio and reasonable volumetric ratio can be generated by selecting the proper design parameters and freestream conditions. Next, the configuration of the multidirectional-curvature waverider with finlets can be constructed (Fig. 3). Finally, the corresponding nondimensional aerodynamic and geometric properties based on the waverider length are calculated, as listed in Table 1.

Governing Equations and Numerical Algorithm

The three-dimensional compressible unsteady form of the Navier–Stokes equations can be written in generalized coordinates and conservation form:

$$\partial_t Q + \partial_\xi (E - E_v) + \partial_\eta (F - F_v) + \partial_\zeta (G - G_v) = 0 \tag{5}$$

where the vector Q represents the conserved variables; E, F, G and E_v, F_v, G_v stand for the inviscid and viscous flux terms, respectively. Also, a calorically perfect gas was assumed, and the viscosity μ is described by Sutherland's law as a function of temperature.

Using an implicit, finite volume, upwind algorithm,[13] the Navier–Stokes equations are solved in conservation form under the generalized coordinate transformation $x^i = [\zeta, \eta, \xi]^t$ with respect to $x_i = [x, y, z]^t$. The governing equations can be rewritten in integral form for a bounded finite volume Ω with its corresponding cell surface boundary $\partial\Omega$:

$$\frac{\partial}{\partial t}\int_{\Omega} Q\,\mathrm{d}v + \oint_{\partial\Omega} [\Phi(\hat{n}) - V(\hat{n})]\,\mathrm{d}s = 0 \tag{6}$$

The approximate Riemann solver of Roe[13] is applied for the numerical representation of the inviscid fluxes. The quantity Q is obtained by means of the interpolation of the primitive variables $q = [\rho, u, v, w, p]^t$ according to monotone upstream-centered schemes for conservation laws. A second-order central difference scheme is used for viscous fluxes, and the thin-layer approximation is made for each direction.

The no-slip, impermeable, and adiabatic wall boundary conditions were imposed in the present calculations. The outer-boundary and initial-flow conditions are specified as freestream flow properties. The waverider configuration is symmetric around the symmetry plane. A second-order interpolation is used to impose the symmetry condition.

Grid Generation

In this study, the following elliptic partial difference equations are used to generate three-dimensional fixed grids[14]:

$$\begin{aligned} \xi_{xx} + \xi_{yy} + \xi_{zz} &= P(\xi, \eta, \zeta) \\ \eta_{xx} + \eta_{yy} + \eta_{zz} &= Q(\xi, \eta, \zeta) \\ \zeta_{xx} + \zeta_{yy} + \zeta_{zz} &= R(\xi, \eta, \zeta) \end{aligned} \tag{7}$$

Basically, they are Poisson equations. The right-hand sides of these equations represent the source terms. By controlling the source terms on surface, a concentration of grid points is attained on the boundary of the waverider. Consequently, the effects of the boundary layer and the shock layer can be captured correctly.

Furthermore, by the variation of control function $D(J)$, more grid points can capture precisely the dramatic change of physical phenomenon around the apex of the body and the leading edges of the finlets, and along the geometric singular line (wing tip). The control function $D(J)$ is defined as

$$D(J) = \frac{1 - \exp[Ep(J_{\text{lead}} - J)]}{1 - \exp[Ep(J_{\text{lead}} - 1)]} \tag{8}$$

where $J = 1, \ldots, J_{\text{lead}}$ and E_p is an adjustable parameter.

As proposed by He and Rasmussen,[10] an adjustable elliptic cone is chosen as the outer boundary. In this study, a nonlinear successive overrelaxation technique is used to accelerate the convergence of grids. The criterion for the convergence of the grid generation is that the maximum error for each iteration is less than 10^{-5}.

Thompson and Warsi[14] contended that the orthogonality of a grid is acceptable if it does not exceed 0.5 radius. By this criterion, the smoothness and orthogonality of grid generation for the waverider should be acceptable. As shown in Fig. 4, an $i \times j \times k = 49 \times 98 \times 90$ grid distribution for the multidirectional-curvature waverider with finlets has been generated successfully. Herein, i, j, and k represent the streamwise, circumferential, and normal directions, respectively.

Results for On-Design Conditions

A numerical analysis is performed for the multidirectional-curvature waverider including finlets, flying at both design Mach number 4 and off-design Mach numbers 2–6. Foremost, at the design condition, the precision and reliability of the analytical estimate are examined. Next, an investigation is made of the variation in flowfields and aerodynamic performance caused by the viscous effects, various flight Mach numbers, and the addition of finlets. A detailed description is provided in the following subsections.

Forebody Portion

In on-design conditions, the pressure contours at several cross planes along the body (Fig. 5) indicate that the shock and relative contour levels of each of the cross sections are similar to others in the forebody. In addition, the surface pressure at the cross plane $x/l_w = 0.72$, which belongs to the forebody, is shown in Fig. 6a. Except near the wing tip, the Euler and HSDT solutions are in good agreement. Moreover, the viscous pressure is very close to the inviscid, since the viscous effect is confined to a well-behaved laminar boundary layer. Furthermore, with viscous interaction, the pressure is slightly larger than in the inviscid case, particularly near the wing tip. However, on addition of finlets, an oscillating surface pressure distribution appears in the finlet region (Fig. 6b). Thus, the flowfields enclosing finlets become very complicated.

To emphasize the influence of the addition of finlets, several particular cross sections along the entire configuration are selected to systematically analyze and discuss the variety of pressures near the surface. The pressure contours at the $x/l_w = 0.72$ cross plane, which belongs to the forebody, are illustrated in Fig. 7a. As found in the available numerical results regarding the waverider's airframe,[8,9,11,12] because of the approximate nature of hypersonic small-disturbance theory and the numerical scheme, the shock is slightly away from the wing tip, and leakage is still not avoidable. Hence, high-pressure leaking from the lower surface to the upper surface occurs and induces a low-pressure zone near the wing tip. In addition, as in previous studies,[9,12] the pressure on the lower surface exhibits an increasing trend near the wing tip, owing to the transverse curvature and viscous interaction there.

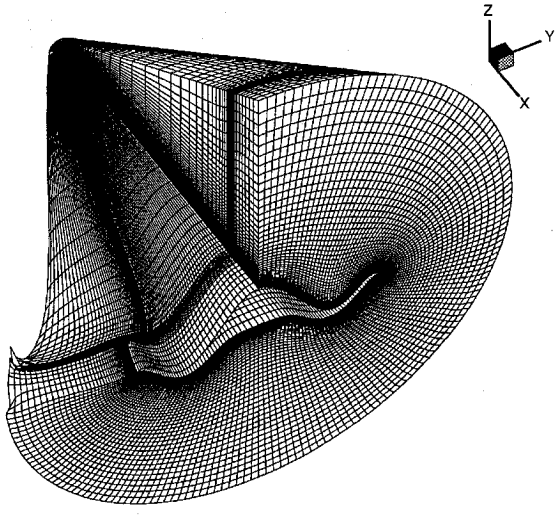

Fig. 4 Three-dimensional grid for MDCWRF: $i \times j \times k = 49 \times 98 \times 90$.

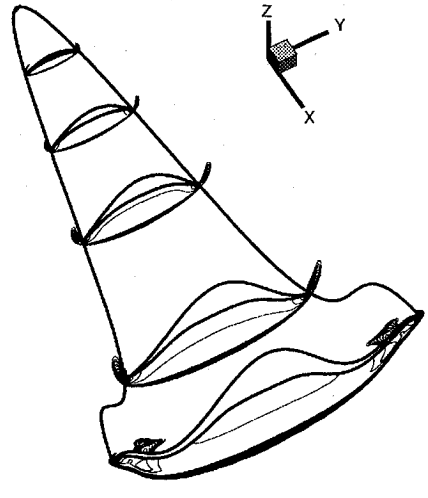

Fig. 5 On-design pressure contours at several cross sections: M_∞ = 4.0; α = 0 deg.

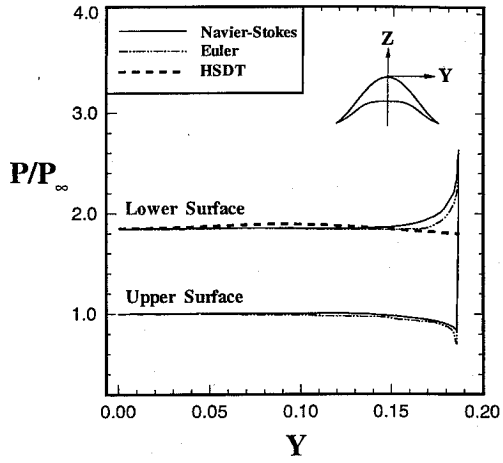

a) x/l_w = 0.72 cross plane

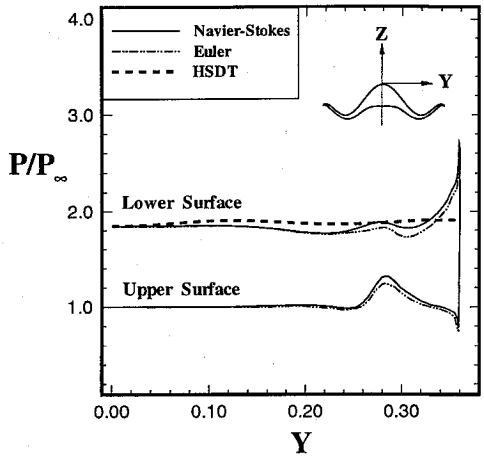

b) Exit flow plane

Fig. 6 On-design surface pressure distribution.

Finlet Portion

Next to the forebody, at the location $x/l_w = 0.84$, the finlets begin to grow and extend sharply out in the transverse direction. Obviously, the geometric variation is so intense beyond this section that the shock development generated by the finlets cannot adapt itself to this abrupt transformation. Therefore, Fig. 7b shows that the shock almost attaches to the finlets, thereby inducing a strong shock-wave–boundary-layer interaction in a downstream transitional plane at $x/l_w = 0.851$. This effect subsequently enhances the pressure on the lower surface of the finlets, and ultimately results in an increase of pressure. Also, no wing-tip leakage occurs in this downstream section.

The growth of finlets in the span direction turns to be mild beyond the $x/l_w = 0.875$ section. However, the shock wave caused by the finlets still increases continuously and separates gradually from the lower surface of the finlets. To the base plane ($x/l_w = 1.0$), the shock-cone angle generated by the finlets has fully developed and merged smoothly into the shock generated by framebody (Fig. 7c). Also, the shock detaches from the surface of the finlets, and the shock-wave–boundary-layer interaction disappears.

The wing-tip leakage of the upstream forebody spreads further to form a higher-pressure zone on the upper surface of the finlets (Figs. 6b and 7c). Also, the high-pressure region, induced by the shock-wave–boundary-layer interaction of the upstream transitional plane spreads further to form higher-pressure zones on the lower surface of the finlets (Figs. 6b and 7c). These zones result in an oscillating pressure distribution on the finlet surfaces, and they expand in size and weaken in strength as the flow moves downstream.

To visualize the flow pattern, under on-design conditions, particles are released from the leading edge of upper surface. Figure 8 shows that the particles flow downstream along the surface of the forebody, and are then slightly deflected to the concave upper surface of the afterbody. Moreover, the particles are jostled away from the region of the high-pressure vortex, and their traces have a

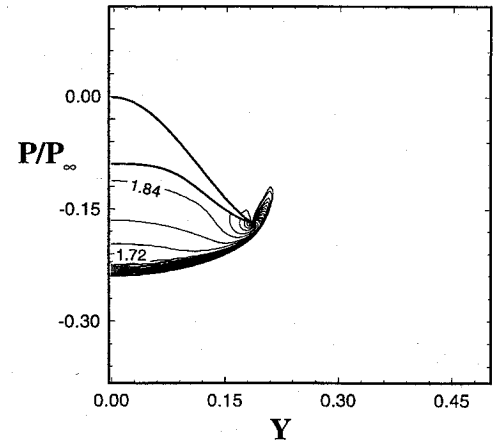

a) x/l_w = 0.72 cross plane

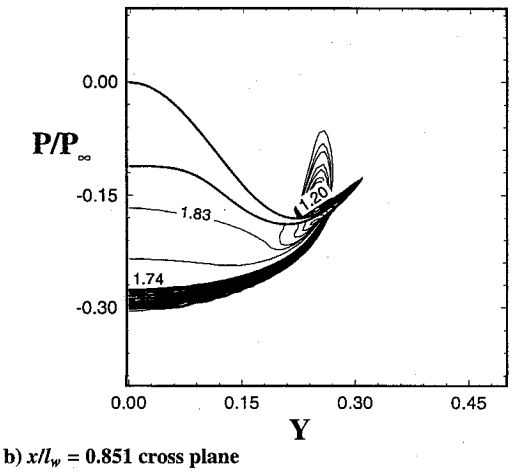

b) x/l_w = 0.851 cross plane

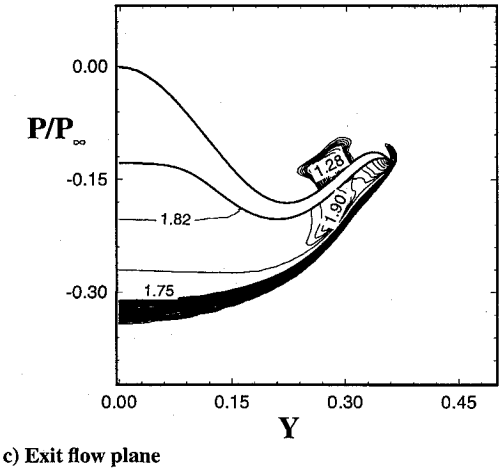

c) Exit flow plane

Fig. 7 On-design pressure contours: M_∞ = 4.0; α = 0 deg.

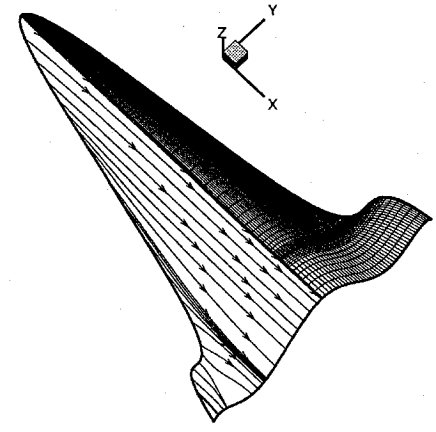

Fig. 8 On-design particle traces on the upper surface.

Table 2 Computational comparisons at on-design conditions (M_∞ = 4.0)

	Inviscid			Viscous		
Type	Euler	HSDT	Error, %	Navier–Stokes	HSDT	Error, %
C_L	0.6488	0.6508	0.3	0.6477	0.6508	0.5
C_D	0.0769	0.0794	3.1	0.0973	0.0990	1.7
$\bar{C}_f$	0	0	0	0.0195	0.0196	0.5
L/D	8.437	8.198	2.9	6.659	6.571	1.4
Δz_{sm}	−0.0739	−0.0735	0.5	−0.0761	—	—

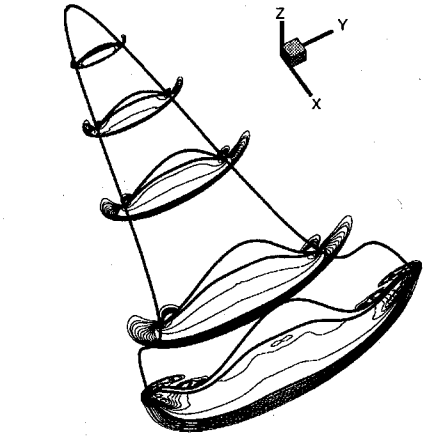

a) M_∞ = 3.0

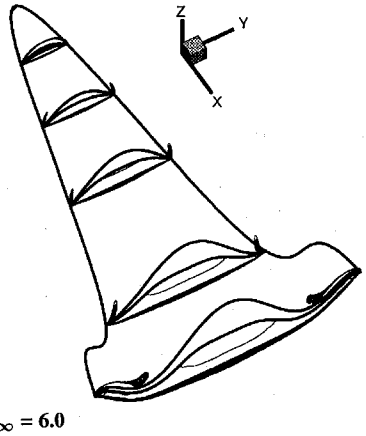

b) M_∞ = 6.0

Fig. 9 Off-design pressure contours at several cross sections.

deflection in the afterbody. In summary, the forebody does maintain the freestream condition, while the afterbody does not.

Aerodynamic Performance

Table 2 lists the on-design L/D, C_L, C_D, $\bar{C}_f$, and static margin calculated by the numerical method and HSDT. In this study, the base drag is ignored and set equal to zero. This table reveals that all of the inviscid and viscous flowfield values predicted by HSDT agree well with the numerical results. As previously mentioned, the viscous flow pressure is close to the inviscid one. Therefore, the lift coefficients for the viscous and inviscid cases are almost identical. A comparison of the viscous with the inviscid numerical results reveals that the skin-friction drag is approximately 20% of the total drag, which is quite different from the 3.14% reported by Liao et al.[8] for the EDCWR. Also, L/D decreases from an inviscid value of 8.437 to a viscous one of 6.659, i.e., a 21% reduction. Hence, we can conclude that viscous effect plays a more prominent role for this slender MDCWRF than it does in the case of an elliptic-cone waverider. Besides, the static margin is more positive than −0.083 for a slender cone.[5] This result validates that the effect of finlets is to improve static stability.

Results for Off-Design Mach Numbers

A flight vehicle cannot always cruise under its on-design conditions. Thus, knowledge of off-design flowfields associated with the

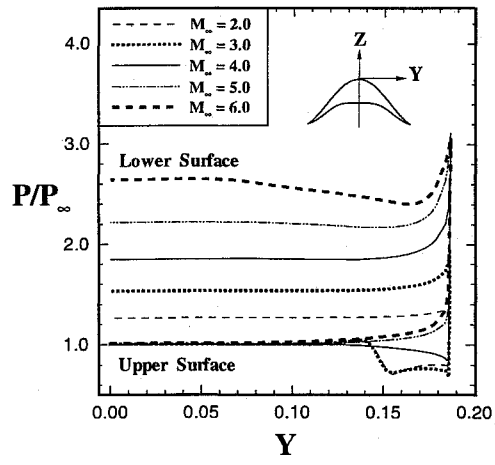

Fig. 10 Off-design surface pressure distribution at x/l_w = 0.72 cross plane.

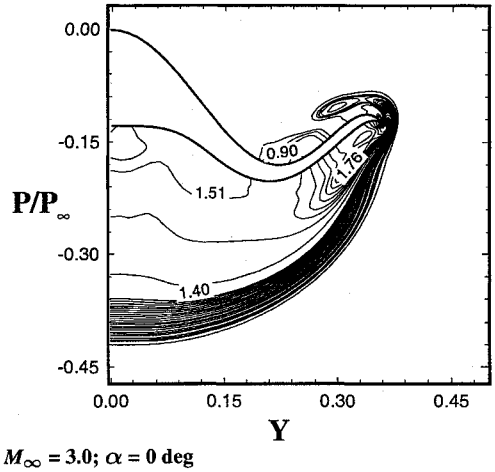

a) M_∞ = 3.0; α = 0 deg

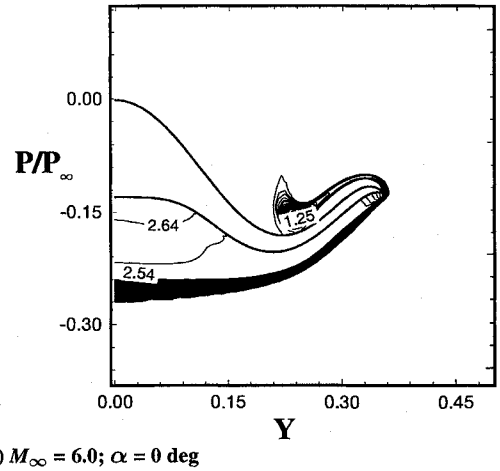

b) M_∞ = 6.0; α = 0 deg

Fig. 11 Off-design pressure contours at the exit flow plane.

waverider is very important. In this section, a waverider flying at Mach numbers ranging from 2 to 6 is examined. This examination provides further insight into the vehicle flight range. The typical pressure contours at several cross planes along the entire body are presented in Figs. 9a and 9b for Mach numbers 3 and 6, respectively. Those figures clearly indicate that the flowfields enclosing the finlets become more complicated and heterogeneous as the Mach number varies.

Figure 10 demonstrates the variation of the surface pressure distribution in the airframe portion, $x/l_w = 0.72$, at various Mach numbers. Figures 9 and 10 indicate that, for the forebody flowfields, the shock becomes weaker and wider when the flight speed is lower than cruising Mach number. In addition, the detachment of shock to the leading edge increases and results in larger wing-tip leakage, which would, in turn, cause a lower pressure zone near the wing tip

Table 3 Aerodynamic properties at off-design Mach numbers

M_∞	C_L	C_D	$\bar{C}_f$	$\bar{C}_f/C_D$	L/D	Δz_{sm}
2.0	1.0014	0.1273	0.0217	0.17	7.867	−0.0629
3.0	0.7953	0.1091	0.0202	0.19	7.245	−0.0726
4.0	0.6477	0.0973	0.0195	0.20	6.659	−0.0761
5.0	0.5631	0.0913	0.0205	0.23	6.170	−0.0713
6.0	0.4981	0.0824	0.0200	0.24	6.044	−0.0686

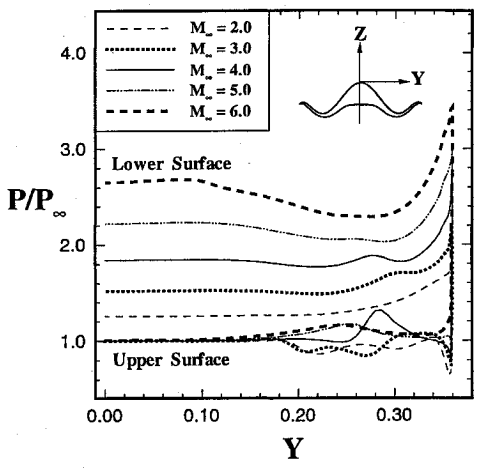

Fig. 12 Off-design surface pressure distribution at the exit flow plane.

of the upper surface (Figs. 9a and 10). On the other hand, the shock becomes stronger and narrower as the flight Mach number increases. Also, on the upper surface of the waverider, a high-pressure region appears near the wing tip instead of the lower pressure (Figs. 9b and 10). On the lower surface, a linear increase of pressure is observed for an increasing Mach number. These assertions have also been reported for previous numerical results[10–12] on the forebody.

In the afterbody region, the off-design pressure contours at the exit flow plane are plotted in Figs. 11a and 11b for Mach numbers 3 and 6, respectively. Also, Fig. 12 shows the pressure distribution for various Mach numbers in the base plane. With an increase in Mach number, a comparison of Fig. 7c with 11b reveals that the high-pressure oscillation, as induced by the wing-tip leakage of the forebody, becomes weaker and shifts toward the symmetry plane on the upper surface (Fig. 12). When the Mach number is lower than the on-design value, instead of a higher-pressure region, a lower-pressure oscillation is found in Figs. 11a and 12.

All the aerodynamic properties at different Mach numbers are tabulated in Table 3 for clarity. This table reveals that the L/D, lift, and drag coefficients decrease monotonically with an increase in the flight Mach number. Also, the contribution of skin friction to total drag increases with Mach number. Notably, these trends correspond well to the numerical simulation for nonconical waveriders performed by Takashima and Lewis.[11] Likewise, the increase in the static margin and slight decrease in L/D show that the waverider with finlets has stable flight performance rather than a dramatic degradation. This stability holds even if the flowfields enclosing the finlets are complicated at different flight Mach numbers.

Conclusions

Three-dimensional, inviscid, and laminar flowfields associated with multidirectional-curvature waveriders including finlets (MD-CWRF) have been presented in this study. Also, this hypersonic vehicle is analyzed for both design Mach 4 and off-design Mach numbers 2–6 by successful simulation of the Euler and Navier–Stokes equations. Results obtained in this study are summarized in the following.

Under on-design conditions, both the inviscid and viscous numerical results correlate well with HSDT's prediction—even for the characteristics of flowfields near the finlets, which deviated from the theoretical assumption. The results validate the precision and reliability of theoretical predictions. Regarding the flow pattern for the present waverider-based vehicle, the flowfields in the forebody still maintain the freestream condition on the upper surface. In the afterbody portion, however, the surface pressure displays an oscillatory distribution because of the wing-tip loss in the forebody and the complex geometry of the finlet region. Moreover, the viscous effect on various aerodynamic performance is evaluated in this study. Its influence on the lift is insignificant, but it is important for the drag of this slender configuration. Under on-design conditions, the skin friction contributes about 20% of the total drag, thereby reducing the L/D by 21%. In addition, the results prove that the static stability can be improved by adding finlets.

Regarding the flight at off-design Mach numbers, in the forebody, the trend of flowfields and the distribution of pressure are similar to previous numerical computations at various flight Mach numbers. As the flight Mach number varies, the flowfields in the finlets region become complicated and heterogeneous. With an increase in flight Mach number, a similar high-pressure oscillation (as mentioned under on-design conditions) is found with a weaker strength. Also, this region is shifted toward the symmetry plane on the upper surface. In the other hand, a low-pressure oscillation appears on the upper surface of the finlets for the waverider flying at a lower Mach number than the design value.

In conclusion, under design and off-design Mach numbers, the lift-to-drag ratio of multidirectional-curvature waveriders with finlets remains large while the static stability is improved. Also, they have stable flight performance even if the flowfields enclosing the finlets are complicated at off-design Mach numbers.

Acknowledgment

The authors would like to thank the National Science Council of the Republic of China for financial support of this work under Contract 83-0424-E-011-050.

References

[1]Eggers, A. J., Jr., Ashley, H., Springer, G. S., Bowles, J. V., and Ardema, M. D., "Hypersonic Waverider Configuration from the 1950's to the 1990's," *Proceedings of the First International Hypersonic Waverider Symposium*, Vol. 1, Univ. of Maryland, College Park, MD, 1990, pp. 1–81

[2]Rasmussen, M. L., "Waverider Configurations Derived from Inclined Circular and Elliptic Cones," *Journal of Spacecraft and Rockets*, Vol. 17, No. 6, 1980, pp. 537–545.

[3]Lin, S. C., and Rasmussen, M. L., "Cone-Derived Waverider with Combined Transverse and Longitudinal Curvature," AIAA Paper 88-0371, Jan. 1988.

[4]Lin, S. C., and Luo, Y. S., "Integrated Inlets for Cone-Derived Waverider with Combined Transverse and Longitudinal Curvature," *Journal of Spacecraft and Rockets*, Vol. 31, No. 4, 1994, pp. 609–614.

[5]He. X., Rasmussen, M. L., and Cox, R. A., "Waveriders with Finlets," *Journal of Aircraft*, Vol. 31, No. 5, 1994, pp. 1135–1142.

[6]Lin, S. C., and Luo, Y. S., "Integrated Design of Hypersonic Waveriders Including Inlets and Tailfins," *Journal of Spacecraft and Rockets*, Vol. 32, No. 1, 1995, pp. 48–54.

[7]Yoon, B. H., and Rasmussen, M. L., "Computational Analysis of Hypersonic Flows Past Elliptic-Cone Waveriders," Univ. of Oklahoma Research Rept. OU-AME-91-2, Jan. 1991.

[8]Liao, J. R., Isacc, K. M., Miles, J. B., and Tsai, B. J., "Navier–Stokes Simulation for Cone-Derived Waverider," *AIAA Journal*, Vol. 30, No. 6, 1992, pp. 1521–1528.

[9]Tsai, B. J., Miles, J. B., and Isacc, K. M., "Computation of Turbulent Flow about Cone-Derived Waverider," AIAA Paper 92-2726, June 1992.

[10]He, X., and Rasmussen, M. L., "Computational Analysis of Off-Design Waveriders," *Journal of Spacecraft and Rockets*, Vol. 31, No. 2, 1994, pp. 345–353.

[11]Takashima, N., and Lewis, M. J., "Navier–Stokes Computation of a Viscous Optimized Waverider," *Journal of Aircraft*, Vol. 31, No. 3, 1994, pp. 383–391.

[12]Lin, S. C., and Shen, M. C., "Computational Simulation of Waverider with Multi-Directional Curvature Flying in Different Mach Numbers," *Journal of the Chinese Society of Mechanical Engineers*, Vol. 16, No. 6, 1995, pp. 565–576.

[13]Roe, P. L., "Approximate Riemann Solvers, Parameter Vectors and Difference Schemes," *Journal of Computational Physics*, Vol. 43, No. 2, 1981, pp. 357–372.

[14]Thompson, J. F., and Warsi, Z. U. A., "Boundary-Fitted Coordinate Systems for Numerical Solution of Partial Differential Equations: A Review," *Journal of Computational Physics*, Vol. 47, No. 1, 1982, pp. 101–108.

K. J. Weilmuenster
Associate Editor